Continuous Surface Matched Filtering: A Finite Dimensional Analysis

Peter J. Smith*, Erfan Khordad†, Rajitha Senanayake†, Justin P. Coon††
* School of Mathematics and Statistics, Victoria University of Wellington, Wellington, New Zealand
† Department of Electrical and Electronic Engineering, University of Melbourne, Melbourne, Australia
†† Department of Engineering Science, University of Oxford, Oxford, UK

***Abstract*—Building on recent trends in multiple-input multiple-output and reconfigurable intelligent surfaces, where densely spaced element arrays are considered, this paper focuses on continuous antenna systems where the receive antenna is modelled as a continuous line (in the one-dimensional case) or a continuous surface (in the two-dimensional case). Considering a spatially-correlated Rayleigh process for the communication channel, we conduct an analytical investigation based on matched filtering. More specifically, we derive an approximated distribution for the instantaneous received signal-to-noise ratio (SNR) at the continuous surface. Furthermore, we derive approximations to the achievable rate, average symbol error rate for M-ary phase shift keying (MPSK) and an upper bound for the achievable rate. We use extensive numerical examples to illustrate the accuracy of our approximation to the SNR distribution as well as the performance analysis.**

***Index Terms*—Continuous surface, signal-to-noise ratio, correlated channels, symbol error rate, achievable rate.**

I. Introduction

The evolution of data traffic in recent years demonstrates an unprecedented growth in demand for high data rate wireless communications [1]. As a result, numerous technologies such as massive Multiple-input multiple-output (MIMO), super-wideband massive MIMO, reconfigurable intelligent surfaces (RISs) and holographic MIMO are being proposed. One common theme among many novel technologies is the trend towards implementing large antennas arrays with tightly packed antenna arrays/elements. A common theme among the above novel technologies is the trend towards implementing large antennas arrays with tightly packed array elements.

MIMO antennas are ubiquitously used in current wireless communication systems to provide the required data rates [2]. With the introduction of fifth generation (5G) wireless communications, there has been great interest in massive MIMO which scales up the number of transmitters or receivers by many orders of magnitude compared to the current state-of-the-art [3], [4], thereby achieving much higher data rates compared to conventional MIMO. Recently, super-wideband massive MIMO systems were proposed in [5] where a large number of antennas are tightly coupled in a compact space. It was shown that one effect of the mutual coupling produced by this tight integration is to widen the operational bandwidth of the system, so that coupling can be turned into an advantage.

At the same time, RIS has gained much research attention in recent years. With RIS, a large number of meta-material-based reflecting elements on the surface, with adjustable phase shifts, are used to reflect the signals toward a desired receiver. This improves the coverage as well as capacity in wireless communications systems [6]. Holographic MIMO systems, on the other hand, are meta-surfaces with a massive number of meta-material elements. Almost the whole surface is used for radiating and sensing in these continuous surfaces, as opposed to traditional MIMO with discrete antenna elements. RISs with numerous meta-elements can also be considered as continuous surfaces but with a different hardware implementation [7], [8].

Continuous surface systems have attracted notable research attention in recent years. In [9], the spatial degrees of freedom and capacity of a continuous surface system were studied for different deployments of user terminals by performing matched filtering (MF). However an infinitely large surface area was considered. MF over a continuous surface with finite dimensions was considered in [10], [11]. The surface was divided into sub-areas corresponding to single-antenna users. Considering an infinite number of sub-areas on the surface, in [10], the uplink data rate of a sub-area was analyzed and in [11], the distribution of the uplink sum-rate was approximated. The interference channel in [10], [11] was modeled by correlated fading due to the correlated multipath environment. However, spatial channel correlation across the continuous surface was not considered in [9]–[11]. However, in practice the spatial correlation across the surface cannot be ignored for continuous surfaces [12], [13].

In this paper, we consider a single antenna user communicating with a receiver equipped with a finite-dimension continuous surface, unlike [9] with infinite dimensions. We consider one continuous surface, unlike [10], [11] that conducted analysis for infinite number of sub-areas on a planar space. The channel model takes into account the spatial channel correlation across the continuous surface. We start with a 1-D case and provide a thorough analysis on the performance of continuous antennas under a general channel model. Based on a gamma approximation, we derive an accurate approximation for the distribution of the instantaneous received signal-to-noise ratio (SNR). To obtain the shape and scale parameters of the gamma distribution, we compute the moments of the instantaneous received SNR. Furthermore, we derive the achievable rate and an upper bound on the achievable rate as well as the average symbol error rate for M-ary phase shift keying (MPSK). Then we extend our results to a 2-D rectangular continuous surface. We present extensive simulation

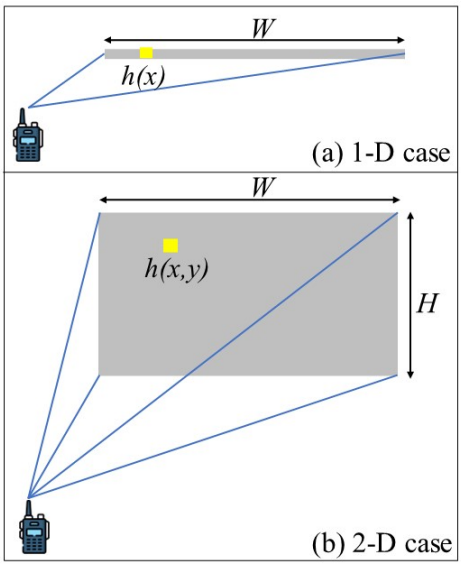

Fig. 1. System model with 1-D and 2-D continuous antenna systems.

results to illustrate the accuracy of our approximated SNR distribution. Furthermore, the analytical expressions for the achievable rate and average symbol error rate show excellent agreement with simulated values. Our results also show that the simple upper bound developed for the achievable rate is very accurate in higher frequency bands.

II. System Model

We consider linear or one-dimensional (1-D) as well as rectangular or two-dimensional (2-D) continuous surfaces separately, as shown in Fig. 1 (a) and (b), respectively. We assume a single antenna user equipment (UE) with channel $h(x)$, $0 \leq x \leq W$, in the linear 1-D case and channel $h(x,y)$, $0 \leq x \leq W$, $0 \leq y \leq H$ in the rectangular 2-D case. As such, the received signal is given by

$$r(x) = h(x)s + n(x), \tag{1}$$

in 1-D and

$$r(x,y) = h(x,y)s + n(x,y), \tag{2}$$

in 2-D, where $n(x)$ and $n(x,y)$ are 1-D and 2-D noise processes and s is the transmitted symbol satisfying $\mathbb{E}\left[|s|^2\right] = E_s$. The noise processes are zero-mean Gaussian with a covariance structure $\mathbb{E}\left[n(x_1)n^*(x_2)\right] = \sigma^2\rho_1(x_1,x_2)$ and $\mathbb{E}\left[n(x_1,y_1)n^*(x_2,y_2)\right] = \sigma^2\rho_2(x_1,y_1,x_2,y_2)$ where $\rho_1(x,x) = \rho_2(x,y,x,y) = 1$, $|\rho_1(.)| \leq 1$ and $|\rho_2(.)| \leq 1$. The channel is assumed to be a Rayleigh process so that $h(x) \sim \mathcal{CN}(0,\beta)$ and $h(x,y) \sim \mathcal{CN}(0,\beta)$ with covariance functions $\mathbb{E}\left[h(x_1)h^*(x_2)\right] = \beta r_1(x_1,x_2)$ and $\mathbb{E}\left[h(x_1,y_1)h^*(x_2,y_2)\right] = \beta r_2(x_1,y_1,x_2,y_2)$. The correlations $r_1(.)$ and $r_2(.)$ satisfy $r_1(x,x) = 1$, $r_2(x,y,x,y) = 1$ and $|r_1(.)| \leq 1$, $|r_2(.)| \leq 1$.

III. One-dimensional Analysis

In this section we consider the 1-D case which is later extended to the 2-D case. Without specifying a particular receiver, let us assume that the surface provides receive filtering at every point via a weighting function $w(x)$. Aggregating the outputs over the surface gives the global output as

$$Z_1 = \int_0^W w^*(x)r(x)dx \triangleq \gamma_1 s + w_1, \tag{3}$$

where $\gamma_1 = \int_0^W w^*(x)h(x)dx$ and $w_1 = \int_0^W w^*(x)n(x)dx$. Hence, the instantaneous received signal-to-noise ratio (SNR) for the surface filtering is:

$$\gamma_s = \frac{E_s|\gamma_1|^2}{\mathbb{E}_n\left[|w_1|^2\right]}, \tag{4}$$

where $\mathbb{E}_n[.]$ represents expectation over the noise process. First, we compute the first two moments of the signal power and evaluate $\mathbb{E}_n\left[|w_1|^2\right]$. Then, we leverage these parameters to develop performance measures for surface filtering.

Let us begin by focusing on the moments of γ_1. From (3), we obtain

$$\mathbb{E}\left[\gamma_1\right] = \int_0^W \mathbb{E}\left[w^*(x)h(x)\right]dx, \tag{5}$$

and

$$\mathbb{E}\left[|\gamma_1|^2\right] = \int_0^W \int_0^W \mathbb{E}\left[w^*(x)h(x)w(x')h^*(x')\right]dxdx'. \tag{6}$$

Next, from (3) we also obtain

$$\begin{aligned}&\mathbb{E}_n\left[|w_1|^2\right]\\ &= \int_0^W \int_0^W \mathbb{E}_n\left[w^*(x)w(x')\right]\mathbb{E}_n\left[n(x)n^*(x')\right]dxdx'\\ &= \sigma^2\int_0^W \int_0^W w^*(x)w(x')\rho_1(x,x')dxdx'.\end{aligned} \tag{7}$$

Further developments of (5)-(7) depends on the precise weighting function implemented across the surface.

To gain better insights, in this paper we consider MF. When MF is applied, $w(x) = h(x)$ and (5)-(7) depend on basic results for correlated Gaussian variables: $\mathbb{E}\left[|h(x)|^2\right] = \beta$, $\mathbb{E}\left[|h(x)|^2|h(x')|^2\right] = \beta^2(1+r_1^2(x,x'))$ and $\mathbb{E}\left[h^*(x)h(x')\right] = \beta r_1(x',x)$. Hence, from (5)-(7), we obtain

$$\mathbb{E}\left[\gamma_1\right] = \beta W, \tag{8}$$

$$\mathbb{E}\left[|\gamma_1|^2\right] = \beta^2\int_0^W \int_0^W (1 + r_1^2(x,x'))dxdx'. \tag{9}$$

Note that for any reasonable choice of a correlation model, (9) is an easily computable integral with a smooth, bounded integrand. For particular correlation models, (9) can often be simplified or solved exactly (see Sec. III-A).

A. Signal-to-Noise Ratio Analysis

We develop an approximation to the SNR distribution using our calculation of the moments above. From (3), we obtain $\gamma_1 = \int_0^W |h(x)|^2dx$. Also, we assume a spatially white noise process, so that $\rho_1(x_1,x_2) = 0$ unless $x_1 = x_2$. Hence, from (7), we obtain $\mathbb{E}_n\left[|w_1|^2\right] = \sigma^2\int_0^W |h(x)|^2dx$, and the instantaneous SNR in (4) takes the simple form

$$\gamma_s = \frac{E_s}{\sigma^2}\int_0^W |h(x)|^2dx = \frac{E_s}{\sigma^2}\gamma_1. \tag{10}$$

Therefore, from (8) and (9) we derive the moments of γ_s as

$$\mathbb{E}\left[\gamma_s\right] = \frac{\beta E_s W}{\sigma^2}, \tag{11}$$

$$\mathbb{E}\left[\gamma_s^2\right] = \frac{\beta^2 E_s^2}{\sigma^4}\int_0^W \int_0^W (1 + r_1^2(x,x'))dxdx'. \tag{12}$$

Motivated by the fact that the gamma distribution accurately approximates sums of exponential variables, e.g., [14], we proceed to approximate γ_s as a gamma random variable. Note that the integral in (10) can be thought of as the limit of a sum of exponential variables. In principle, improved approximations can be obtained by computing higher order moments [15], but our results in Section V show that the two-moment approximation is satisfactory.

We now compute the second moment in (12). Here, we consider correlation models where $r_1(x,x')$ depends only on the spatial separation, so that $r_1(x,x') = r_{1S}(|x-x'|)$. Thus, after some manipulation, (12) can be written as

$$\mathbb{E}\left[\gamma_s^2\right] = \frac{\beta^2 E_s^2}{\sigma^4}\left(W^2 + 2\int_0^W (W-x) r_{1S}^2(x)dx\right). \tag{13}$$

Now consider the particular spatial fading correlation model, $r_{1S}(x) = J_0(2\pi x/\lambda)$ [16], [17], where $J_k(.)$ is the k-th order Bessel function of the first kind. Therefore, (13) becomes

$$\begin{aligned}&\int_0^W (W-x) J_0^2(2\pi x/\lambda)dx \\ &= W\int_0^W J_0^2(\alpha x)dx - \int_0^W x J_0^2(\alpha x)dx,\end{aligned} \tag{14}$$

where $\alpha = 2\pi/\lambda$. For convenience, we define the terms in (14) by $A(\alpha, W) = W\int_0^W J_0^2(\alpha x)dx$ and $B(\alpha, W) = \int_0^W x J_0^2(\alpha x)dx$. We derive $A(\alpha, W)$ as follows by defining $z = \alpha x$ and using standard integrals,

$$\begin{aligned}A(\alpha, W) &= \frac{W}{\alpha}\int_0^{\alpha W} J_0^2(z)\,dz \\ &= W^2\, {}_2F_3\left(\frac{1}{2}, \frac{1}{2}; 1; 1; \frac{3}{2}; -\alpha^2 W^2\right),\end{aligned} \tag{15}$$

where ${}_2F_3$ is the hypergeometric function [18, Sec. 9.14]. Also we calculate the function $B(\alpha, W)$ by defining $t = x/W$ as follows [18, 6.521.1],

$$B(\alpha, W) = W^2\int_0^1 t J_0^2(\alpha W t)dt = W^2\frac{1}{2}J_1^2(\alpha W). \tag{16}$$

Referring to (13)-(16), we compute the second moment as

$$\mathbb{E}\left[\gamma_s^2\right] = \frac{\beta^2 E_s^2 W^2}{\sigma^4}\left(1 + 2\ {}_2F_3(\frac{1}{2}, \frac{1}{2}; 1; 1; \frac{3}{2}; -\alpha^2 W^2) - J_1^2(\alpha W)\right). \tag{17}$$

Therefore from (11) and (17), we calculate the SNR variance:

$$Var\left[\gamma_s\right] = \frac{\beta^2 E_s^2 W^2}{\sigma^4}\left(2\ {}_2F_3(\frac{1}{2}, \frac{1}{2}; 1; 1; \frac{3}{2}; -\alpha^2 W^2) - J_1^2(\alpha W)\right). \tag{18}$$

Finally, we compute the the shape and scale parameters of our gamma approximation for the SNR as $a = (\mathbb{E}\left[\gamma_s\right])^2/Var[\gamma_s]$ and $\delta = \mathbb{E}\left[\gamma_s\right]/Var[\gamma_s]$ and therefore our approximated gamma distribution is $\gamma_s \sim G(a, \delta)$ with probability density function (PDF) $p_{\gamma_s}(\gamma)$. The accuracy of our gamma approximation is demonstrated in Section V, using (11) and (18) to compute the gamma parameters.

B. Upper Bound on the Achievable Rate

Here, we give a simple upper bound on the mean achievable rate, R, based on our calculations of the first moment of γ_s. Using Jensen's inequality [19] and referring to (11) gives,

$$\mathbb{E}\{R\} \le R^{\text{up}} = \log(1 + \mathbb{E}\{\gamma_s\}) = \log\left(1 + \frac{\beta E_s W}{\sigma^2}\right). \tag{19}$$

C. Achievable Rate Analysis

For our approximate gamma distribution, $\gamma_s \sim G(a, \delta)$, the achievable rate is given as

$$\mathbb{E}\{R\} = \int_0^\infty \log_2(1+\gamma) p_{\gamma_s}(\gamma)d\gamma. \tag{20}$$

By substituting the gamma PDF into (20), we obtain

$$\mathbb{E}\{R\} = \frac{\delta^a}{\ln(2)\Gamma(a)}\int_0^\infty \ln(1+\gamma)\gamma^{a-1}e^{-\delta\gamma}d\gamma, \tag{21}$$

where $\Gamma(.)$ is the gamma function. Finally, we compute the expression in (21) as [20]

$$\mathbb{E}\{R\} = \frac{1}{\ln(2)\Gamma(a)} G_{3,2}^{1,3}\left(\begin{matrix}1-a & 1 & 1\\ 1 & 0 & \end{matrix}\middle|\, \frac{1}{\delta}\right), \tag{22}$$

where $G(.)$ is the Meijer G function that can be calculated using the built-in Matlab function meijerG. Note that (22) is an approximation to the mean rate using the gamma model.

D. Symbol Error Rate Analysis

We calculate the average symbol error rate for M-ary phase shift keying (MPSK), using our gamma approximation. The average symbol error rate can be written as [19]

$$\bar{P_s} = \frac{1}{\pi}\int_0^{\frac{M-1}{M}\pi}\int_0^\infty e^{\frac{-g\gamma_s}{\sin^2\phi}} p_{\gamma_s}(\gamma)\ d\gamma d\phi, \tag{23}$$

where $g = \sin^2(\pi/M)$. Based on the definition of the moment generating function (MGF) and using the MGF of our approximated gamma distribution $M_{\gamma_s}(s)$, (23) becomes

$$\begin{aligned}\bar{P_s} &= \frac{1}{\pi}\int_0^{\frac{M-1}{M}\pi} M_{\gamma_s}\left(\frac{-g}{\sin^2\phi}\right)d\phi \\ &= \frac{1}{\pi}\int_0^{\frac{M-1}{M}\pi}\left(1 + \frac{g}{\delta\sin^2\phi}\right)^{-a}d\phi.\end{aligned} \tag{24}$$

The integral in (24) is computed as [21]

$$\begin{aligned}\bar{P_s} = &\frac{\Gamma(a+\frac{1}{2})}{2\sqrt{\pi}\Gamma(a+\frac{1}{2})} M_{\gamma_s}(-g)\, {}_2F_1\left(a, \frac{1}{2}; a+1; \frac{1}{1-g/\delta}\right) \\ &+ \frac{1}{\pi}\cos(\pi/M) M_{\gamma_s}(-g) \\ &+ F_1\left(\frac{1}{2}, a, \frac{1}{2}-a; \frac{3}{2}; \frac{\cos^2(\pi/M)}{1-g/\delta}, \cos^2(\pi/M)\right),\end{aligned} \tag{25}$$

where ${}_2F_1$ is a hypergeometric function and F_1 is the Appell hypergeometric function. Note that (25) is an approximation to the SER using the gamma model.

IV. Two-dimensional Analysis

We now extend our analysis to the 2-D case where the continuous surface has a rectangular shape as illustrated in Fig. 1(b). Assuming spatially white noise, the development in equations (3)-(10) can be simply followed in the 2-D case to give the weighting function, $w(x,y) = h(x,y)$ and the instantaneous received SNR , $\widetilde{\gamma}_s$, is given by

$$\widetilde{\gamma}_s = \frac{E_s}{\sigma^2}\int_0^W \int_0^H |h(x,y)|^2 dydx = \frac{E_s}{\sigma^2}\widetilde{\gamma}_1. \tag{26}$$

Our approach to approximate the SNR distribution as a gamma distribution from Section III is still valid as $\widetilde{\gamma}_1$ has the same interpretation as an integral of a Chi-squared process. Hence, we compute the first two moments of $\widetilde{\gamma}_s$. The mean is given by

$$\mathbb{E}\left[\widetilde{\gamma}_s\right] = \frac{E_s}{\sigma^2}\beta WH = \frac{E_s}{\sigma^2}\beta A, \tag{27}$$

where A is the surface area. For the second moment, similar to (12), we have

$$\mathbb{E}\left[\widetilde{\gamma}_s^2\right] = \frac{\beta^2 E_s^2}{\sigma^4}\int_0^W\int_0^H\int_0^W\int_0^H (1+r_2^2(x,y,x',y'))dy'dx'dydx. \tag{28}$$

Referring to (27)-(28) we obtain

$$Var\left[\widetilde{\gamma}_s\right] = \frac{\beta^2 E_s^2}{\sigma^4}\int_0^W\int_0^H\int_0^W\int_0^H r_2^2(x,y,x',y')dy'dx'dydx. \tag{29}$$

In general, (29) depends on the particular correlation model adopted and cannot be simplified. However, substantial simplification occurs for common models where the correlation is isotropic or separable in the x,y domain. Assuming the correlation is isotropic, then $r_2(x,y,x',y') = g(\sqrt{(x-x')^2+(y-y')^2})$. Introducing the change of variables $u = x-x'$ and $v = y-y'$, allows (29) to be re-expressed as

$$Var[\widetilde{\gamma}_s] = \frac{4\beta^2 E_s^2}{\sigma^4}\int_{u=0}^W\int_{v=0}^H (W-u)(H-v)g^2(\sqrt{u^2+v^2})dvdu. \tag{30}$$

Then, changing to polar coordinates gives

$$Var[\widetilde{\gamma}_s] = \frac{4\beta^2 E_s^2}{\sigma^4}\int_{r=0}^{\sqrt{W^2+H^2}} rg^2(r) \int_{\theta\in S(r)} WH - Wr\sin\theta - Hr\cos\theta + r^2\sin\theta\cos\theta d\theta dr, \tag{31}$$

where $S(r)$ denotes the range of θ and we derive $S(r)$ as

$$S(r) = \begin{cases} [0,\pi/2] & r \le H \\ [0,\sin^{-1}(\frac{H}{r})] & H < r \le W \\ [\sin^{-1}(\frac{H}{r}),\cos^{-1}(\frac{W}{r})] & W < r \le \sqrt{W^2+H^2}. \end{cases} \tag{32}$$

Note that (32) assumes that $W \ge H$ but in the isotropic case results for $W < H$ are simply obtained by switching W and H. Each of the integrals over θ in (31) is trivial so we combine (31)-(32) to calculate the variance as

$$\begin{aligned} Var[\widetilde{\gamma}_s] = \frac{4\beta^2 E_s^2}{\sigma^4}\Bigg\{ &\int_0^H rg^2(r)\left[WH\frac{\pi}{2} - (W+H)r + \frac{r^2}{2}\right]dr \\ &+ \int_H^W rg^2(r)\left[WH\sin^{-1}\left(\frac{H}{r}\right) + W\sqrt{r^2-H^2} - Wr - \frac{H^2}{2}\right]dr \\ &+ \int_W^{\sqrt{W^2+H^2}} rg^2(r)\left[WH\left(\cos^{-1}\left(\frac{W}{r}\right) - \sin^{-1}\left(\frac{H}{r}\right)\right)\right. \\ &\left. + \frac{W^2+H^2+r^2}{2} - W\sqrt{r^2-H^2} - H\sqrt{r^2-W^2}\right]dr\Bigg\}. \end{aligned} \tag{33}$$

Note that (33) is an integral over a finite region for a smooth, bounded function. Thus, numerical integration is straightforward using built-in software.

Now, using (27) and (33), a gamma approximation can be fitted to $\widetilde{\gamma}_s$. As shown in Sec. V, the gamma fit is excellent in 2-D. Whilst not shown here due to page limitations, the rate bound, the mean rate and the SER results for the 1-D case can all be used in the 2-D case, by the simple expedient of using (27) and (33) for the SNR moments.

V. Numerical Results

In this section we provide numerical examples to illustrate the accuracy of our analysis. In simulations we adopt commonly used frequency bands in 4G and 5G including 0.5 GHz, 5.8 GHz and 28 GHz [22]. We first present results for the 1-D case. In all cases, the classic spatial correlation model $J_0(2\pi d/\lambda)$ is used, where d is the spatial separation. In the simulations, the integral representations for γ_s and $\widetilde{\gamma}_s$ are simulated by the standard Riemann sum approach. Hence, the surface is broken into discrete points where the number of points is selected to be large enough so that no change in the integral is observed if more points are used.

Figs. 2 and 3 show the cumulative distribution function (CDF) of the instantaneous receive SNR along with the approximated gamma distribution. Fig. 2 is for a fixed length $W = 600$ mm and the frequencies are changed as 0.5 GHz, 5.8 GHz and 28 GHz. Fig. 3 shows results for a fixed frequency of 5.8 GHz and W is changed to 200 mm, 400 mm and 600 mm lengths. As can be seen, for all of the above cases the gamma approximation is an excellent fit to the simulation. Hence, the approach can deliver accurate outage values and the subsequent plots demonstrate that this also leads to accurate rate and SER results.

Figs. 4 and 5 compare the upper bound on achievable rate in (19) with the simulated mean rate, for a range of lengths and SNRs, respectively. As can be seen from the results, the bound is still reasonable at 0.5 GHz but is almost exact for higher frequencies. This property follows from the fact the spatial correlation reduces for smaller wavelengths, considering the spatial fading correlation model adopted in Section III. Hence, more averaging occurs over the surface and the SNR stabilizes making the upper bound a good approximation.

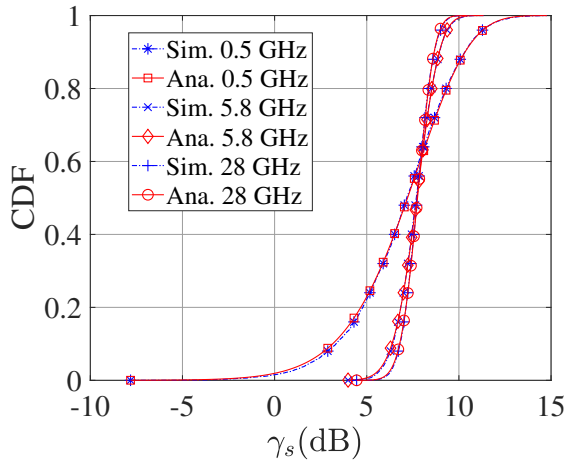

Fig. 2. Cumulative distribution function of γ_s for fixed length $W = 600$ mm, $\frac{E_s}{\sigma^2} = 10$ dB, $\beta = 1$.

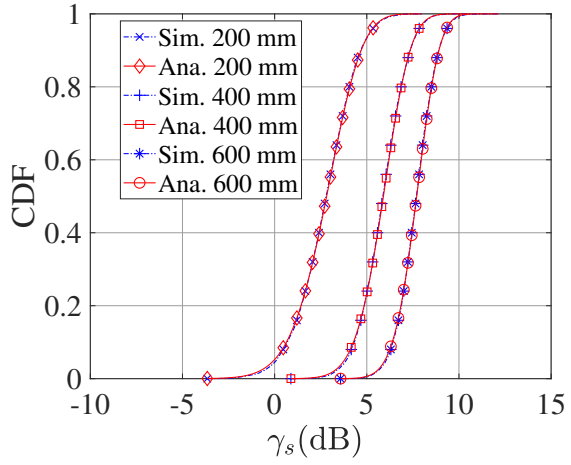

Fig. 3. Cumulative distribution function of γ_s for fixed frequency 5.8 GHz, $\frac{E_s}{\sigma^2} = 10$ dB, $\beta = 1$.

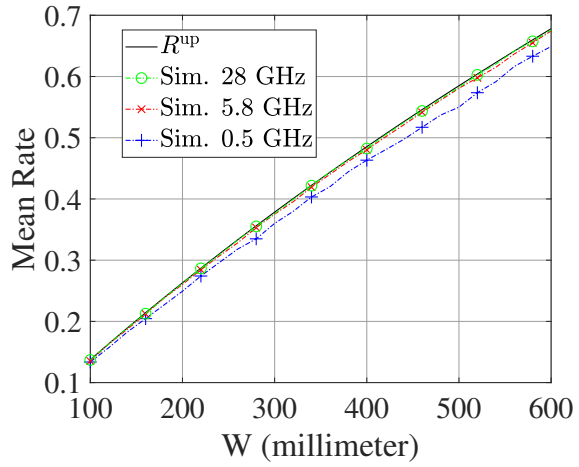

Fig. 4. Mean rate versus the length W for $\frac{E_s}{\sigma^2} = 0$ dB, $\beta = 1$.

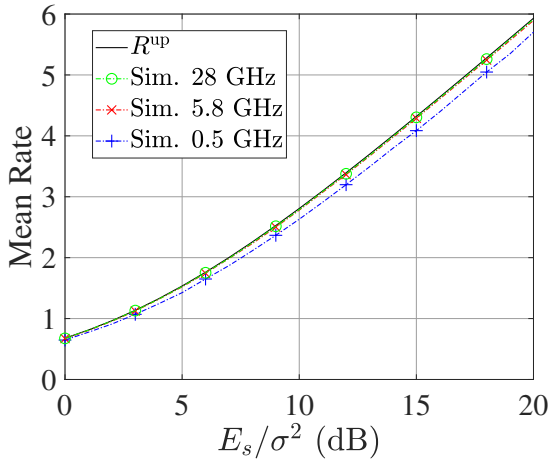

Fig. 5. Mean rate versus $\frac{E_s}{\sigma^2}$ for fixed length W= 600 mm, $\beta = 1$.

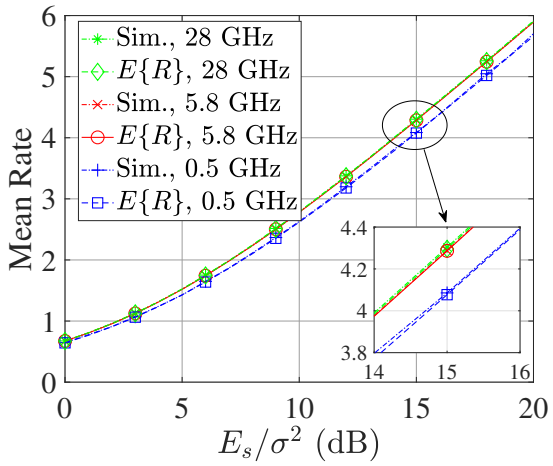

Fig. 6. Average achievable rate versus $\frac{E_s}{\sigma^2}$ for W= 600 mm and $\beta = 1$.

In Fig. 6, we plot the mean rate versus $\frac{E_s}{\sigma^2}$. The analytical achievable rate results are generated using (22). From the plot we observe that the gamma approximation is in close agreement with the simulated values. Since the mean rate is largely driven by the mean SNR, which is constant for all frequencies, there is little variation in rate across the frequencies.

In Fig. 7, we plot the average symbol error rate (SER) versus $\frac{E_s}{\sigma^2}$. The analytical average SER is computed by our results in (25) with the simulated average SER computed using a Monte-Carlo simulation. We consider 3 different modulation methods, namely, BPSK, QPSk and 16-PSK. The figure shows that the results from our analytical expression are extremely accurate at all SNRs and for all modulation methods considered.

Finally, for the 2-D case, it suffices to show that the gamma approximation for the SNR is accurate, since rate and SER results immediately follow from the gamma model as explained in Section IV. Fig. 8 shows the CDF of our approximate gamma distribution for $\widetilde{\gamma}_s$ and the simulated CDF,

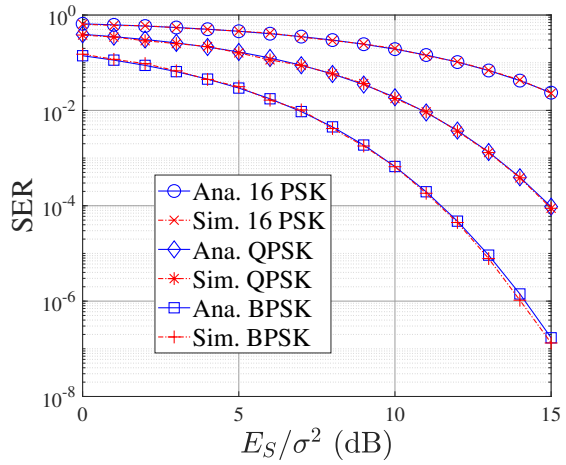

Fig. 7. Symbol error rate for fixed length W= 600 mm and frequency 5.8 GHz, $\beta = 1$.

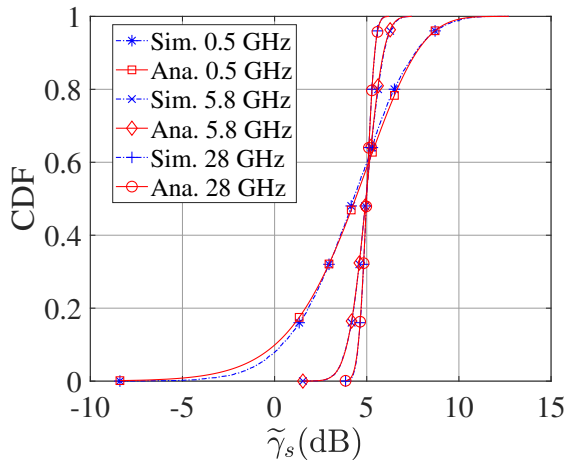

Fig. 8. Cumulative distribution function of $\widetilde{\gamma}_s$ for 2-D surface, with $W = 300$ mm, $H = 200$ mm, $\beta = 1$ and $\frac{E_s}{\sigma^2}$ is set so that $\mathbb{E}[\widetilde{\gamma}_s] = 5$dB.

for a fixed height and width of the rectangular surface. As can be seen, the gamma distribution in the 2-D case is an excellent match to the simulated distribution. Due to page limitations, rate and SER results are not presented for the 2-D case.

VI. Conclusion

We have focused on a finite dimensional continuous antenna system and performed MF at the receiver. We considered both the one-dimensional case as well as the two-dimensional case. We have considered a channel model that takes into account the spatial channel correlation across the continuous antenna. Leveraging the gamma approximation, we have also provided analytical expressions for the achievable rate, an upper bound on the achievable rate and the average symbol error rate for M-ary phase shift keying. Our results for 4G and 5G frequency bands show that the gamma approximation for the SNR distribution leads to an extremely accurate performance analysis in terms of both rate and SER.

References

[1] M. Z. Chowdhury, M. Shahjalal, S. Ahmed, and Y. M. Jang, "6G wireless communication systems: Applications, requirements, technologies, challenges, and research directions," *IEEE Open Journal of the Communications Society*, vol. 1, pp. 957–975, 2020.

[2] A. J. Paulraj and T. Kailath, "Increasing capacity in wireless broadcast systems using distributed transmission/directional reception (DTDR)," US Patent 5 (599A), 345, Sep. 1994.

[3] T. L. Marzetta, E. G. Larsson, H. Yang, and H. Q. Ngo, *Fundamentals of Massive MIMO*. Cambridge University Press, 2016.

[4] T. L. Marzetta, "Massive MIMO: An introduction," *Bell Labs Technical Journal*, vol. 20, pp. 11–22, 2015.

[5] M. Akrout, V. Shyianov, F. Bellili, A. Mezghani, and R. W. Heath, "Super-wideband massive MIMO," *IEEE Journal on Selected Areas in Communications*, vol. 41, no. 8, pp. 2414–2430, 2023.

[6] Y. Liu, X. Liu, X. Mu, T. Hou, J. Xu, M. Di Renzo, and N. Al-Dhahir, "Reconfigurable intelligent surfaces: Principles and opportunities," *IEEE Communications Surveys & Tutorials*, vol. 23, no. 3, pp. 1546–1577, 2021.

[7] C. Huang, S. Hu, G. C. Alexandropoulos, A. Zappone, C. Yuen, R. Zhang, M. D. Renzo, and M. Debbah, "Holographic MIMO surfaces for 6G wireless networks: Opportunities, challenges, and trends," *IEEE Wireless Communications*, vol. 27, no. 5, pp. 118–125, 2020.

[8] R. Deng, Y. Zhang, H. Zhang, B. Di, H. Zhang, H. V. Poor, and L. Song, "Reconfigurable holographic surfaces for ultra-massive MIMO in 6G: Practical design, optimization and implementation," *IEEE Journal on Selected Areas in Communications*, vol. 41, no. 8, pp. 2367–2379, 2023.

[9] S. Hu, F. Rusek, and O. Edfors, "Beyond massive MIMO: The potential of data transmission with large intelligent surfaces," *IEEE Transactions on Signal Processing*, vol. 66, no. 10, pp. 2746–2758, 2018.

[10] M. Jung, W. Saad, Y. Jang, G. Kong, and S. Choi, "Performance analysis of large intelligent surfaces (LISs): Asymptotic data rate and channel hardening effects," *IEEE Transactions on Wireless Communications*, vol. 19, no. 3, pp. 2052–2065, 2020.

[11] ——, "Reliability analysis of large intelligent surfaces (LISs): Rate distribution and outage probability," *IEEE Wireless Communications Letters*, vol. 8, no. 6, pp. 1662–1666, 2019.

[12] O. T. Demir, E. Bjrnson, and L. Sanguinetti, "Channel modeling and channel estimation for holographic massive MIMO with planar arrays," *IEEE Wireless Communications Letters*, vol. 11, no. 5, pp. 997–1001, 2022.

[13] L. Wei, C. Huang, G. C. Alexandropoulos, W. E. I. Sha, Z. Zhang, M. Debbah, and C. Yuen, "Multi-user holographic MIMO surfaces: Channel modeling and spectral efficiency analysis," *IEEE Journal of Selected Topics in Signal Processing*, vol. 16, no. 5, pp. 1112–1124, 2022.

[14] N. K. Kundu and M. R. McKay, "RIS-assisted MISO communication: Optimal beamformers and performance analysis," in *2020 IEEE Globecom Workshops (GC Wkshps)*, 2020, pp. 1–6.

[15] P. J. Smith, R. Senanayake, and P. A. Dmochowski, "How accurate is your gaussian/gamma approximation?" *IEEE Wireless Communications Letters*, vol. 7, no. 5, pp. 804–807, 2018.

[16] D. Gesbert, T. Ekman, and N. Christophersen, "Capacity limits of dense palm-sized MIMO arrays," in *Global Telecommunications Conference, 2002. GLOBECOM '02. IEEE*, vol. 2, 2002, pp. 1187–1191 vol.2.

[17] D.-S. Shiu, G. Foschini, M. Gans, and J. Kahn, "Fading correlation and its effect on the capacity of multielement antenna systems," *IEEE Transactions on Communications*, vol. 48, no. 3, pp. 502–513, 2000.

[18] I. S. Gradshteyn and I. M. Ryzhik, *Table of Integrals, Series, and Products*, 7th ed. Burlington, MA, USA: Academic, 2007.

[19] A. Goldsmith, *Wireless Communications*. Cambridge University Press, 2005.

[20] V. K. Dwivedi and G. Singh, "A novel moment generating function based performance analysis over correlated Nakagami-m fading channels," *J. Comput. Electron.*, vol. 10, no. 4, p. 373381, Dec 2011.

[21] H. Shin and J. H. Lee, "On the error probability of binary and M-ary signals in Nakagami-m fading channels," *IEEE Transactions on Communications*, vol. 52, no. 4, pp. 536–539, 2004.

[22] W. H. Bailey, B. R. T. Cotts, and P. J. Dopart, "Wireless 5G radiofrequency technology-An overview of small cell exposures, standards and science," *IEEE Access*, vol. 8, pp. 140 792–140 797, 2020.